

High-quality-factor space–time metasurface for free-space power isolation at near-infrared regime

Raana Sabri[✉] and Hossein Mosallaei*

Northeastern University, Department of Electrical and Computer Engineering, Boston, Massachusetts, United States

Abstract. Space–time metasurfaces are promising candidates for breaking Lorentz reciprocity, which constrains light propagation in numerous practical applications. There is a substantial difference between carrier and modulation frequencies in space–time photonic metasurfaces that leads to negligible spatial pathway variation of light and weak nonreciprocal response. To surmount this obstacle, herein, the design principle of a high-quality-factor space–time gradient metasurface is demonstrated at the near-infrared regime that increases the lifetime of photons and allows for strong power isolation by lifting the adiabaticity of modulation. The all-dielectric metasurface consists of an array of silicon subwavelength gratings (SWGs) that are separated from distributed Bragg reflectors by a silica buffer. The resonant mode with ultrahigh quality-factor exceeding 10^4 is excited within the SWG, which is characterized as magnetic octupole and features strong field localization. The SWGs are configured as multijunction p–n layers, whose multigate biasing with time-varying waveforms enables modulation of carriers in space and time. The proposed nonreciprocal metasurface is exploited for free-space optical power isolation by virtue of modulation-induced phase shift. It is shown that under time reversal and by interchanging the directions of incident and observation ports, power isolation of ≈ 35 dB can be maintained between the two ports in free space.

Keywords: space–time metasurface; high-Q resonator; optical nonreciprocity; active photonic platform.

Received Aug. 10, 2023; revised manuscript received Oct. 13, 2023; accepted for publication Nov. 6, 2023; published online Dec. 11, 2023.

© The Authors. Published by SPIE and CLP under a Creative Commons Attribution 4.0 International License. Distribution or reproduction of this work in whole or in part requires full attribution of the original publication, including its DOI.

[DOI: [10.1117/1.APN.2.6.066008](https://doi.org/10.1117/1.APN.2.6.066008)]

1 Introduction

Metasurfaces, two-dimensional and planar arrays of subwavelength scatterers, are of particular interest for sculpting the wavefront of light through imprinting local space-variant abrupt phase discontinuities to the incoming wavefronts.^{1,2} They have demonstrated unprecedented capability in a wide range of applications, such as anomalous reflection,³ pulse shaping,^{4,5} polarization control,^{6,7} and beam focusing.^{8,9} The ultrathin and compact footprint of the metasurfaces as well as their great fabrication feasibility have made them very promising for optical component miniaturization and on-chip integration. The initial efforts toward the development of metasurfaces employed passive scatterers, whose optical responses are controlled by tailoring their geometrical parameters. The static nature of passive

metasurfaces specifies their application to the initial functionality that they were designed for and ties the postfabrication tunability of their optical response. Many emerging applications, including light detection and ranging, optical communication, augmented/virtual reality, and imaging, call for a new class of metasurfaces with the capability of achieving versatile dynamic response to shape the wavefronts at will.

An immense effort has been devoted to realizing active metasurfaces through dynamic manipulation of their constituent building blocks.^{10–13} Different stimulation mechanisms have been used to alter the resonant properties of the unit cells by triggering the refractive index of active material integrated into the metasurface or mechanically reconfiguring the dimension or position of the individual unit cells. In particular, electrical gating, optical pumping, thermal annealing, and current-induced heating can be employed for this purpose.^{14–19} Thus far, quantum-confined Stark effects in multiple quantum wells,^{20,21}

*Address all correspondence to Hossein Mosallaei, hosseinm@ece.neu.edu

molecular phase transitions in vanadium dioxide (VO₂) or germanium antimony telluride,²² reorientation of molecules in liquid crystals,²³ ionic transparent, and carrier-induced field effects in semiconductors, i.e., silicon (Si), gallium arsenide,^{24,25} transparent conducting oxides (TCOs),^{26–30} indium arsenide (InAs),^{31,32} and atomically thin transition metal dichalcogenides,^{33,34} have been leveraged for index modulation. Among these tuning mechanisms, the free-carrier-induced effects in doped semiconductors have yielded great promise for active tuning thanks to higher modulation frequencies (up to several gigahertz), continuous tunability, and lower power consumption compared to techniques based on the Pockels effect or waveguide modulators based on lithium niobate. One major obstacle toward application of this method is the negligible strength of electrorefraction that occurs within a nanometer-thin active layer and results in small refractive index modulation.^{26,35} To partly surmount this challenge, the dual-gated biasing technique has been proposed, which enhances the mode overlap with the active region by increasing the volume of the accumulation/depletion layers.³⁶ In addition, the background doping density in semiconductors, such as TCO, and InAs can be judiciously adjusted such that the epsilon near-zero phenomenon takes place within the active regions, resulting in strong electric field confinement and large tunability of the optical response. Increasing the light–matter interaction through careful design of the metasurface platform is an alternative method to achieving large amplitude/phase modulation at the output. Transitioning the resonant mode between the over- and undercoupled regimes,^{37–39} employing the Kerker’s resonators with two degenerate modes,^{23,25,40} or utilizing the resonators with ultrahigh quality- $(Q-)$ factor for increasing the lifetime of photons⁴⁰ can be used to strengthen the mode overlap with the active tunable medium and yield strong light–matter interaction.

The free-carrier-induced field effect in moderately doped semiconductors, such as Si offers the ability to alter the refractive index within the entire material volume rather than being limited to the ultrathin accumulation/depletion layers. This can be maintained by configuring the host Si resonator into p–i–n/p–n junctions through doping the horizontal/vertical directions. Nevertheless, the maximum attainable refractive index change in such semiconductors is small and typically on the order of 10^{-3} to 10^{-2} at the near-infrared (NIR) regime,^{20,35,40} which hinders wide modulation of light due to the small spectral shift of the resonance. As such, a proper design paradigm with an ultrahigh Q -factor should be implemented to enhance the field confinement and lifetime of photons within the resonator. Thus far, several structures have been proposed for increasing the light–matter interactions at the nanoscale level. In particular, the widely used methods for the realization of high Q -factor modes are built upon the Fabry–Perot cavity resonators,⁴¹ whispering-gallery mode platforms,^{42,43} and guided mode resonators.^{44,45} More recently, the concept of bound states in the continuum (BICs) has triggered extensive attention, since it is capable of yielding a Q -factor up to 10^8 in extended systems, such as photonic crystal slabs or plasmonic and dielectric metasurfaces.^{40,46} Although for any platform comprising regular materials, where the permittivity and permeability are neither zero nor infinite, BICs can only be excited if the dimension is infinite, by modifying the parameters of a finite system to follow its infinite counterpart, quasi-BICs (QBICs) can be supported. Despite the ultrahigh Q -factor that ensures a large change in the optical response of the resonators in response to index modulation,

they cannot be employed for designing the gradient metasurfaces. This is because the index contrast between the neighboring elements of the phase gradient metasurfaces leads to the emergence of epsilon-QBIC mode in systems with a broken symmetry in their permittivity.⁴⁷ An alternative promising technique to boost the Q -factor of a resonator is engineering its dimension to support higher-order Mie resonances.⁴⁸ Similar to their dipolar counterparts, the higher-order Mie modes leverage the confined field distribution that enables local wavefront manipulation while featuring a sufficiently high Q -factor that is obtained thanks to the reduction of radiative losses. Such characteristics make them great candidates for designing dynamically tunable phase gradient metasurfaces with wide modulation range of the scattering properties, and the refractive index modulation remains negligible.

Despite the fruitful progress, the performance of the phase gradient metasurfaces is constrained by Lorentz reciprocity. It is desirable to break the reciprocity in order to achieve full-duplex communication for increasing the link capacity,^{49–51} power isolation, and circulation^{52–55} that have vital importance for optical communication, laser feedback systems, nonreciprocal waveguide walls, nonreciprocal quantum state mediation, illusion cloaks, Faraday isolators, and power dividers.^{56–59} Magneto-optical effects have been traditionally used for breaking the reciprocity by imparting a different momentum over the waves propagating in forward and backward directions. In this case, the permittivity tensor of the magneto-optic material exhibits a nonsymmetric response upon applying the DC magnetic field.⁶⁰ However, these materials are lossy and bulky, which prohibits them from being integrated into the photonic circuits. Alternatively, space–time metasurfaces can be exploited for realizing magnetless nonreciprocity through circumventing the symmetry constraints upon introducing the spatiotemporal modulation. In fact, by introducing the space–time phase discontinuities to the interface of metasurfaces, they are no longer bounded by Lorentz reciprocity.^{51,61,62} In Ref. 61, the concept of nonreciprocal wavefront engineering is experimentally demonstrated at microwaves, in which the nonreciprocity arises due to imposing drastically different phase gradients during the up/downconversion. In this case, the isolation response of more than 20 dB is attained by modulating the unit cells with phase-delayed tones applied to the varactors. Alternative approaches based on nonlinear materials and Weyl semimetals are exploited for inducing nonreciprocity as well.⁶³ Nevertheless, the former technique is limited by its substantial energy consumption, while the latter employs bulky multilayer configurations.

Moving beyond microwave frequencies to the infrared and visible regimes allows for high-speed platforms in free-space communication due to higher frequencies of the carrier signal. In another context, the concept of photonic transitions between two nonlocal modes by time-modulated metasurfaces for optical power isolation and circulation has been demonstrated.⁵² In this approach, using opposite phases for frequency upward and downward transitions, the nonreciprocal response is acquired. However, the restriction is imposed on the frequencies of the two optical modes and the isolation is limited between two specific directions set by the dispersion of the supported modes. The arguably major challenge faced by nonreciprocal space–time metasurface paradigms at the NIR regime is that only a negligible change is imprinted in the spatial pathway of light at the fundamental frequency and higher-order sidebands, under time reversal. As a result, the weak power isolation level is

obtained between the two directions. The underlying reason is the substantial difference between the carrier and modulation frequencies. In this case, for a space–time metasurface operating at the adiabatic regime, the wavelength of the scattered light shifts by undergoing a frequency conversion at the same spatial pathway; however, the power isolation is considerably smaller because of the same frequency conversion performance.

In this paper, we propose and numerically demonstrate a robust method to obtain a strong power isolation in free space using a space–time gradient metasurface at NIR frequencies. For this purpose, we lift the adiabaticity of modulation by designing the ultrahigh Q -factor space–time metasurface that increases the lifetime of the photons such that the time scale of modulation becomes comparable with the optical oscillation of the resonator. The metasurface motif consists of a periodic repetition of amorphous silicon (a -Si) subwavelength grating (SWG), on a silica (SiO_2) buffer, where the entire structure is backed by a distributed Bragg reflector (DBR). The dimension of the SWG is judiciously adjusted to support higher-order Mie mode with the Q -factor exceeding 10^4 , which allows for local manipulation of the resonant properties of light. The SWGs are configured as multijunction p–n layers along the vertical direction to enable spatiotemporal index modulation based on carrier redistributions under the application of time-varying bias voltage. It has been demonstrated that in the nonadiabatic regime, the frequency conversion performance of the space–time metasurface is substantially different for up- and downconverted sidebands under time reversal, even though the spatial pathway of light is identical. This ensures a strong optical power isolation in free space between any two arbitrary directions. By implementing a progressive phase delay across the space–time metasurface, the direction of the normally incident light (port 1) is steered toward the desired angle of 20 deg (port 2) upon upconversion. Under time reversal, the incoming light from port 2 undergoes upconversion and is steered to the initial spatial pathway at port 1. Nonetheless, due to the nonadiabatic modulation, the amplitude of the reflected power at port 1 is significantly suppressed, and normalized power isolation over 35 dB is maintained.

2 Ultrahigh Q -factor Resonant All-Dielectric Metasurface

Subwavelength high-index dielectric resonators with geometries such as grating, disk, and cuboid support Mie resonances. Thus far, the all-dielectric configurations supporting electric and magnetic dipolar modes have been widely used in designing metasurfaces by satisfying the first/second Kerker’s condition to suppress the backward/forward scattering, giving rise to the transmission/reflection.^{23,25,35,64} Nevertheless, the Q -factor of dipolar modes is not sufficiently high to provide the desired spectral shift by exploiting the refractive index change in the order of $\Delta n = 0.01$. Recently, higher-order Mie-type modes have been used in several contexts to excite high Q -factor resonances by increasing the overall dimension of the resonator.^{46,65} In Ref. 48, a Huygens metasurface paradigm that consists of all-dielectric cuboids is proposed that leverages the higher-order Mie resonance to achieve two-dimensional static beam steering. In this regard, the major challenge is to keep the unit cell dimension as compact as possible to avoid the undesired artifacts at the optical response. However, reducing the resonator size and keeping the operating wavelength unchanged, results in

the excitation of lower-order Mie-type modes with higher radiative losses, and consequently lower Q -factor.

The schematic of space–time nonreciprocal metasurface is pictorially illustrated in Fig. 1. We consider a 1D array of a -Si SWG that is separated from the DBR through an SiO_2 buffer. The DBR consists of four pairs of Si/ SiO_2 stacks with Si as the topmost layer. The SWG is configured as three alternative pairs of p–n junctions along the vertical direction. The electrical biasing of this structure is enabled by application of time-varying signal into the SWGs, where p-type and n-type regions serve as the contact electrodes (see inset of Fig. 1). First, we consider the optical response of the unbiased metasurface when it is illuminated by the normally incident TE-polarized light (electric field along the y axis). For this purpose, the material properties of the undoped a -Si and SiO_2 are, respectively, extracted from the experimental data in Refs. 48 and 66, whereas the p- and n-doped Si layers are characterized by the Drude-plasma model as⁶⁷

$$\Delta n_{\text{Si}} = -(e^2 \lambda^2 / 8\pi^2 c^2 \epsilon_0 n_0)(N/m_e^* + P/m_h^*), \quad (1)$$

$$\Delta k_{\text{Si}} = -(e^3 \lambda^3 / 16\pi^3 c^3 \epsilon_0 n_0)(N/m_e^{*2} \mu_e + P/m_h^{*2} \mu_h). \quad (2)$$

In the above equations, e is the electron charge, λ is the operating wavelength, ϵ_0 and n_0 are the permittivity of free space and nominal refractive index of undoped silicon, $m_e^* = 0.27m_0$ and $m_h^* = 0.39m_0$ are the effective mass of the electrons and holes with m_0 being the electron mass, $\mu_e = 80 \text{ cm}^2/\text{V s}$ and $\mu_h = 60 \text{ cm}^2/\text{V s}$ are the electron and hole mobility, and N and P are the carrier densities of electrons and holes, respectively. The p- and n-type regions are uniformly doped with the moderate carrier concentrations of $N = P = 10^{18} \text{ cm}^{-3}$ that can be practically obtained with the current state-of-the-art nanofabrication techniques. The geometrical parameters of the metasurface are optimized to excite the localized and high- Q mode within the SWG that affords a steep phase swing at the NIR regime. The thicknesses of the alternating Si/ SiO_2 pairs in DBR configurations correspond to the effective quarter-wavelength in the high-index contrast materials with refractive indices identical to $n_{\text{SiO}_2} = 1.452$ and $n_{\text{Si}} = 3.487$ at $1.55 \mu\text{m}$. The structural parameters of the metasurface are revealed in the caption of Fig. 1.

The recent advances in the nanofabrication technology have made the fabrication of the proposed device feasible using the chemical vapor deposition (CVD) and electron-beam lithography (EBL).^{41,68,69} First, the DBR structure with four pairs of Si/ SiO_2 quarter-wave stacks should be deposited over the glass substrate using plasma-enhanced chemical vapor deposition (PECVD). Next, the SiO_2 dielectric spacer and an a -Si layer should also be deposited on the sample by PECVD. To form the SWGs, the top a -Si layer should be then patterned by EBL and dry-etched in plasma. It is worth mentioning that the p–n multijunctions have been widely used in tandem solar cells and vertical-cavity surface-emitting lasers.⁷⁰ To implement the layered SWGs, sputtering techniques can be used, wherein boron and phosphorous dopants (B^+ and P^-) are utilized for achieving the desired background carrier distribution across the vertical direction by diffusion and ion implementation.⁷¹

The optical response of the proposed metasurface is studied within the framework of rigorous space–time coupled-wave analysis (RSTWA), which enables analytical simulation of

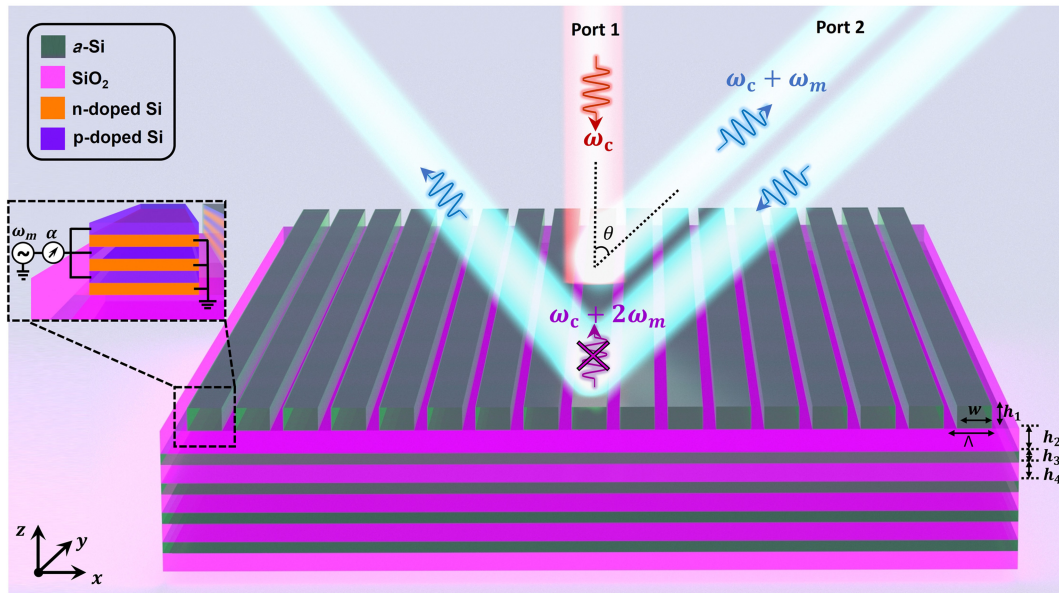


Fig. 1 Conceptual demonstration of light interaction with space–time gradient nonreciprocal metasurface. The metasurface comprises a periodic arrangement of *a*-Si SWG over the SiO_2 substrate that is backed by a four-layer DBR. The optimized dimensions are as follows (units in nm): $w = 853$, $h_1 = 684$, $h_2 = 749$, $h_3 = 104$, $h_4 = 266$, and $\Lambda = 1007$. The incoming TE-polarized light with the frequency ω_c (electric field along the SWG) from port 1 is coupled to port 2 upon upconversion, whereas the incident light coming from port 2 is strongly suppressed after upconversion when coupled to port 1. Therefore, the free-space ports 1 and 2 are isolated. Close-up: the SWG that is configured as three pairs of p–n junctions and the multigate biasing scheme. The modulation is enabled by applying the time-varying signal with the modulation frequency ω_m and RF phase shifters to induce the required phase gradient across the metasurface.

space–time metasurfaces without making any assumption on the frequency of modulation.⁷² RSTWA is the extension of Fourier-based rigorous coupled-wave analysis, which solves the Maxwell equations by expanding them on the basis of plane waves for structures with both spatial and temporal variations. In this technique, the scattered fields are expanded in terms of space–time Fourier harmonics defined by the spatial and temporal periodicities of the structure and the relations between the incident and scattered fields are computed by transforming the periodic spatiotemporal profile of refractive index to the spectral domain. To start, we have obtained the metasurface optical response in the absence of any time modulation; the results are shown in Fig. 2. For this aim, the number of temporal diffraction orders in the RSTWA solver is adjusted to zero, and the Fourier modes along the spatial dimension are carefully chosen to ensure the convergence of the results. To validate the accuracy of the RSTWA simulations, we have compared them against the full-wave simulation results obtained by COMSOL Multiphysics and the details are expressed in Sec. S1 in the [Supplementary Material](#). We have further studied the reflection spectra of the DBR consisting of different pairs and the sensitivity of the optical mode to the incident angle in Secs. S2 and S3 in the [Supplementary Material](#), respectively. Figure 2(a) depicts the reflection amplitude of the metasurface as functions of the incident wavelength and the width (w) of SWG when it varies in the range of 600–900 nm, and h_1 is fixed at 684 nm. On the other hand, the spectral variations of the reflection coefficient are shown in Fig. 2(b) as a function of SWG height h_1 , when it is increasing from 400 to 700 nm,

where w is adjusted to 853 nm. The results clearly indicate the emergence of two branches of the resonant modes that are marked by red and black circles, respectively. In both figures, the black circles correspond to the high- Q resonant modes, and the red branch indicates the reflection dips for the modes with relatively low Q -factors. The size of the circles is proportional to the Q -factor of the supported modes, whose approximate values are depicted in the insets of Figs. 2(a) and 2(b). The Q -factors of the supported modes on black and red branches are calculated; the results are illustrated in Sec. S4 in the [Supplementary Material](#). By moving over the black branch, the mode exhibits linewidth narrowing and therefore, an increase in the Q -factor. The highest Q -factor is maintained at the anticrossing region between two branches at around 1312 nm, whose value reaches the maximum of $\approx 16,000$ that corresponds to the supercavity mode, as shown in Fig. 1(a). This is while, for the red branch with moderately low- Q mode, the Q -factor that is calculated as ≈ 2000 remains almost unchanged by altering w . In an analogy to this case, one can observe that along the black branch in Fig. 2(b), an increase in the Q -factor is achieved for h_1 in the range of 600 to 630 nm and 660 to 700 nm and the maximum Q -factor of $\approx 20,000$ is maintained. Similarly, the red branch corresponds to the low- Q mode and the Q -factor of the resonant mode varies between 900 and 3000 for different values of h_1 . To complete the characterization of the highlighted resonant modes, the near-field distribution of the x component of the magnetic field is depicted for typical values of w and h_1 along with the low- Q and high- Q branches in Figs. 2(a) and 2(b). It is noticeable that at the anticrossing point, the field is extremely

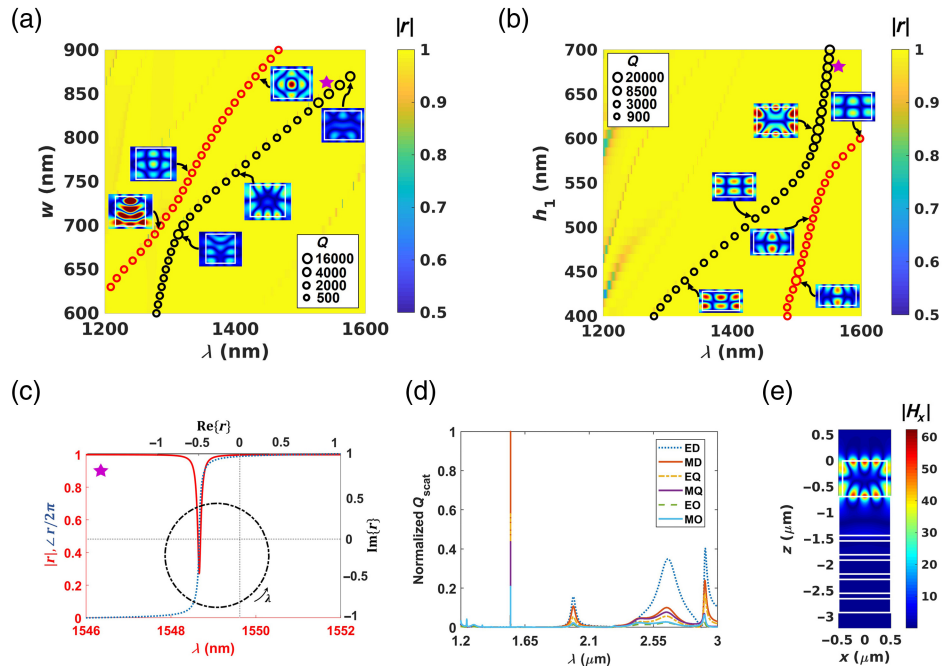


Fig. 2 Simulated characteristics of all-dielectric high- Q time-invariant metasurface under normal illumination of TE-polarized light. The spectral distribution of the metasurface reflection amplitude as functions of (a) width (w) when h_1 is fixed at 684 nm and (b) height (h_1) when w is set to 853 nm. The peak positions and the Q -factors of the two anticrossing modes are shown by black (high- Q mode) and red (low- Q mode) circles. The size of the circles is proportional to the Q -factor levels such that larger circles correspond to high- Q resonances. The insets show the magnetic near-field maps within the SWG cross section for different dimensions at their operating wavelengths over the low- Q and high- Q branches. (c) The amplitude (red) and phase (blue) of the reflected light as a function of incident wavelength when w and h_1 are fixed to 853 and 684 nm, respectively. The alternative x and y axes correspond to the real and imaginary parts of the complex reflection coefficient that illustrates a circle trajectory while covering all four quadrants that ensure 2π phase swing. (d) Multipolar contribution of the scattering cross section of the SWG. (e) Near-zone distribution of the magnetic field within the metasurface cross section at the resonant wavelength of 1548 nm, which confirms excitation of higher-order Mie mode corresponding to the magnetic octupole.

confined within the SWG resonator with the small radiation loss that is the underlying reason for the ultrahigh Q -factor at this point. At slightly higher widths with respect to the mode at the anticrossing point [Fig. 2(a)], it is observed that the energy leaks out of the resonator, resulting in reduction of the Q -factor and an increase in the radiation efficiency. The red branches in both Figs. 2(a) and 2(b) are governed by the lower-order Mie-type modes, as discussed in Ref. 43. In addition, from the results in Figs. 2(a) and 2(b), one can observe that the resonant mode on the black branch strongly depends on w , while it is less sensitive to h_1 . Specifically, when there is a 150 nm change in the width and height of the SWG (w and h_1 are altered within the intervals 720 to 870 nm and 550 to 700 nm), the resonant mode experiences a spectral shift of 233 and 57 nm, respectively. As such, an almost fourfold larger spectral shift is noticed for width variation compared to the height when they both are varying in the same range. The greater sensitivity of the resonant mode to the width of resonator compared to its height is the characteristic of Mie-type resonances, which are formed by the multiple reflections from the left and right interfaces of the resonator. This is while the Fabry–Perot mode is established based on the multiple reflections from the resonator top and bottom interfaces and

therefore are more sensitive to height variations. The reflection amplitude and phase of the metasurface unit cell are calculated at the point denoted by magenta pentagonal marker in Figs. 2(a) and 2(b), which corresponds to $w = 853$ nm and $h_1 = 684$ nm; the result is shown in Fig. 2(c). The high- Q resonant mode can be identified from the steep and highly dispersive spectral phase accumulation of 2π within <1 nm wavelength interval, whose Q -factor reaches 11,876 at 1548 nm. It is worth mentioning that although the loss of a -Si is negligible at the NIR regime, the extreme light–matter interaction at the high- Q resonator gives rise to amplitude attenuation at the resonant wavelength. The real and imaginary parts of the reflection coefficient at this point are plotted at the alternative x and y axis of Fig. 2(c). The reflection coefficient shows a circle trajectory by progressing over the spectral wavelength that covers all four quadrants of the complex plane. This ensures a full 2π spectral phase. Nevertheless, the distance of the points on the circumference from the origin varies, which shows the nonuniform reflection amplitude due to the loss. It should be noted that the excitation of the resonator can be generalized to TM polarization as well. In this case, the avoided crossing of the modes is not always required for exciting the high- Q resonances. However, it is

shown that the interelement coupling between the adjacent unit cells is significant under TM polarization in comparison to TE, which leads to cross talk and undesired sidelobes.^{73–75}

In order to get better insight into the radiative properties of the resonant modes, we employ the multipole decomposition up to the fourth order, tied by electric and magnetic octupoles, to calculate the contribution of each multipole in the scattering response. For this purpose, we have conducted a theoretical analysis based on multipole decomposition method developed for light scattering.^{76–78} In this method, the total electric fields over the resonators composing the metasurface induced by the incident light are calculated, and then the multipole moments of the resonators are extracted following their definition,^{79,80} in which the current density is replaced by the induced polarization vector. The detailed formulation regarding the computation of the multipole moments is indicated in Sec. S5 in the [Supplementary Material](#). Figure 2(d) shows the normalized scattering cross section as a function of incident wavelength over a wide range, and the contribution of the multipole moments at the output response. It is shown that the lower-order modes, i.e., electric and magnetic dipoles, are dominant at the longer wavelengths, where the periodicity of the unit cell is $\approx 1/4$ of the operating wavelength. The Q -factor of the dipolar modes is low, as is clear from Fig. 2(d). As a result, achieving a dynamic wide phase/amplitude modulation via the index changes induced by electro-optical carrier effects is limited. At shorter wavelengths and around $1.55 \mu\text{m}$, the excitation of high- Q modes can be noticed. They correspond to the higher-order Mie-type resonances as the size of the resonator increases with respect to the wavelength. At the wavelength 1548 nm, the contributions of electric and magnetic quadrupoles (EQ and MQ), as well as magnetic octupole (MO) are dominant. Nevertheless, as discussed earlier, the field confinement of MO is higher in comparison to the EQ and MQ, which makes its scattering efficiency smaller. As such, MO represents a decreased scattering cross section at 1548 nm, as can be verified from Fig. 2(d). To provide a fair comparison in terms of scattering efficiency, we have extracted the amplitude of the multipole moments in the same metric, normalized them to the maximum magnitude, and depicted the results in Fig. S5 in the [Supplementary Material](#). The contribution of multipoles reveals that the response is dominated by the MO moment at 1548 nm, confirming the nature of the resonant mode as a magnetic octupole. To further elaborate on the origin of the resonance, the near-field distribution of the x component of the magnetic field is demonstrated in Fig. 2(e). As expected, the near-field pattern illustrates the excitation of a resonant mode that is characterized as a magnetic octupole and is mainly localized within the SWG. Nevertheless, a field enhancement between the adjacent metasurface unit cells that indicates the inter-resonator coupling of the elements can be seen and can lead to undesired artifacts manifested as sidelobes. However, the magnetic field amplitude localized within the SWG is at least twice the interemitter coupling. It should be noted that our proposed metasurface paradigm supports an ultrahigh- Q mode over a subwavelength unit cell. This is unlike the metasurfaces that enable the excitation of guided-mode resonances or QBICs, which offer the Q -factors almost at the same order, while they require larger footprints for supporting in-plane propagation of the photons along the array before leaking out to free space. Although high- Q metasurfaces allow us to obtain wide modulation of optical response by a subtle change of the refractive index, they are highly sensitive to small fabrication

tolerances of the structural parameters, as shown in Figs. 2(a) and 2(b). Another limiting factor in designing ultrahigh- Q metasurfaces is the ohmic loss of the materials. The ohmic loss substantially reduces the Q -factor of the metasurface and prohibits us from further increasing the Q -factor, as shown in Fig. 2(c). Alternative loss origin raised from fabrication imperfections can further reduce the Q -factor of the resonator.⁸¹ In addition, as is observed in Fig. 2(e), although the field distribution is mainly confined within the resonator, the interelement coupling between the adjacent unit cells is not negligible compared to the plasmonic resonators. The nearest-neighbor coupling occurs along the phase gradient direction and therefore results in deviation of the obtained phase from the desired one, and local phase errors can arise from the coupling between the adjacent SWGs. It is worth mentioning that high- Q modes usually suffer from low radiation efficiency due to the strong confinement of the energy. In Sec. S6 in the [Supplementary Material](#), we have evaluated the radiation performance of the magnetic octupole mode and compared its result with an electric dipole mode with a relatively low Q -factor.

3 Space–Time Metasurface Platform

In this section, we study the space–time metasurface paradigm for optical power isolation by introducing time modulation into the system. When the incident light with the angular frequency ω_c interacts with the space–time metasurface, the scattered light undergoes a frequency transition, and higher-order sidebands are generated at the integer multiples of the modulation frequency ω_m ($\omega_n = \omega_c \pm n\omega_m$, where $n \in \mathbb{Z}$). The modulation frequency of the electro-optically tunable metasurfaces can be specified through the RC time constant of their constituent elements and is estimated to be at the order of several hundreds of gigahertz, that is, at least 3 orders of magnitude smaller than the carrier frequency at the NIR regime. This limits the metasurface analysis to the adiabatic regime of modulation, wherein the spatial pathway of light remains almost unchanged for the fundamental frequency and the up- and downmodulation under time reversal. Nevertheless, for the metasurfaces with high Q -factor, similar to our proposed design, the order of magnitude difference between the carrier and modulation frequencies is compensated. In this case, the Q -factor of the resonator is $>11,000$, and the carrier frequency is at the NIR regime; therefore, the lifetime of the photons trapped in the SWG enters the nanosecond range and becomes comparable with the modulation cycle.⁸² This renders the modulation process to be in the nonadiabatic regime. Throughout this paper, we have adjusted the modulation frequency at 55 GHz, which is consistent with the experimental results for the Si-based electro-optical resonators⁷¹ and can be maintained by keeping the metasurface footprint, driver electronics, and wiring as compact as possible to reduce the RC time constant.

Here the design goal is to obtain a nonreciprocal response by the space–time metasurface for achieving optical power isolation in free space. Basically, this can be yielded by imparting the desired momentum for photonic transitions between the fundamental frequency and higher-order sidebands by optimizing the modulation waveform. By using the optimized waveform, the input power is mainly transforms into the into the desired sideband and the undesired mixing products are suppressed. The output spectrum with the desired spectral diversity and efficiency of the sidebands dictates the temporal response of the scattered fields at the steady state, which can be expressed as

$$E_i(t) = E_0 \exp(i\omega_c t), \quad (3)$$

$$\begin{aligned} E_r(t) &= E_0 |r(t)| \exp[i\angle r(t)] \exp(i\omega_c t) \\ &= \sum_{n=-\infty}^{\infty} c_{n,r} \exp[i(\omega_c + n\omega_m)t], \end{aligned} \quad (4)$$

where E_i and E_r stand for the incident and reflected electric fields, E_0 expresses the amplitude of the incident field, $r(t)$ is the time-dependent reflection coefficient, and $c_{n,r}$ is the frequency domain complex amplitude of the reflected field at the n 'th-order sideband that can be obtained by Fourier transform of the time-domain reflection coefficient. In order to achieve the desired nonreciprocal response at the output spectrum, the inverse design and optimization methods should be employed for obtaining the complex modulation waveforms with strong time-reversal asymmetry (i.e., a sawtooth-like pattern).^{83,84} However, these methods are time-consuming, and, as discussed earlier, the spatial pathway of light at different sidebands cannot be sufficiently changed to impart nonreciprocity. Lifting the adiabaticity of modulation offers a pathway to attain a noticeable conversion from the fundamental to higher-order frequencies under time reversal and substantially change the spatial pathway of light, without making any effort to optimize the modulation waveform. Throughout this paper, we have considered a sinusoidal modulation waveform to study the response of the space–time metasurface, unless otherwise stated.

To realize the refractive index modulation within the SWG upon introducing the sinusoidal waveform, the electrorefraction in the multijunction p–n layers is exploited. The carrier modulation in the *a*-Si p–n junctions has been previously used in optical modulators.^{25,85,86} To implement this method as the modulation mechanism of the space–time metasurface, we have divided the SWG into six sublayers along the vertical direction, where the alternative sublayers are uniformly doped by moderate hole and electron carriers with the concentrations of $P = 10^{18} \text{ cm}^{-3}$ and $N = 10^{18} \text{ cm}^{-3}$, respectively. The sublayers are arranged as three pairs of p–n junctions with the order of p–n–p–n–p–n from top to bottom, as depicted in the inset of Fig. 1, where the thickness of each p- and n-type region is $h_1/6 = 114 \text{ nm}$. The p-doped and n-doped regions can be connected to the low-resistance contact pads from the edge of the metasurface, and then they can be wire-bonded to the biasing circuit board. To characterize the electro-optical response of the p–n junctions to external modulation, we have calculated the carrier dynamics within the SWG and then linked the results to the optical properties of the p- and n-type regions through the Drude-plasma model described by Eqs. (1) and (2). The Lumerical device solver is utilized to calculate the bias-dependent carrier distribution of p–n junctions, which self-consistently solves the Poisson and drift-diffusion equations via the finite-element method. The profile of the modulation as a function of time that is applied to the metasurface is depicted in Fig. 3(a). It is a simple sinusoidal function that can be expressed as $V(t) = V_{\text{DC}} + \Delta V \sin(\omega_m t)$, where V_{DC} is the average of

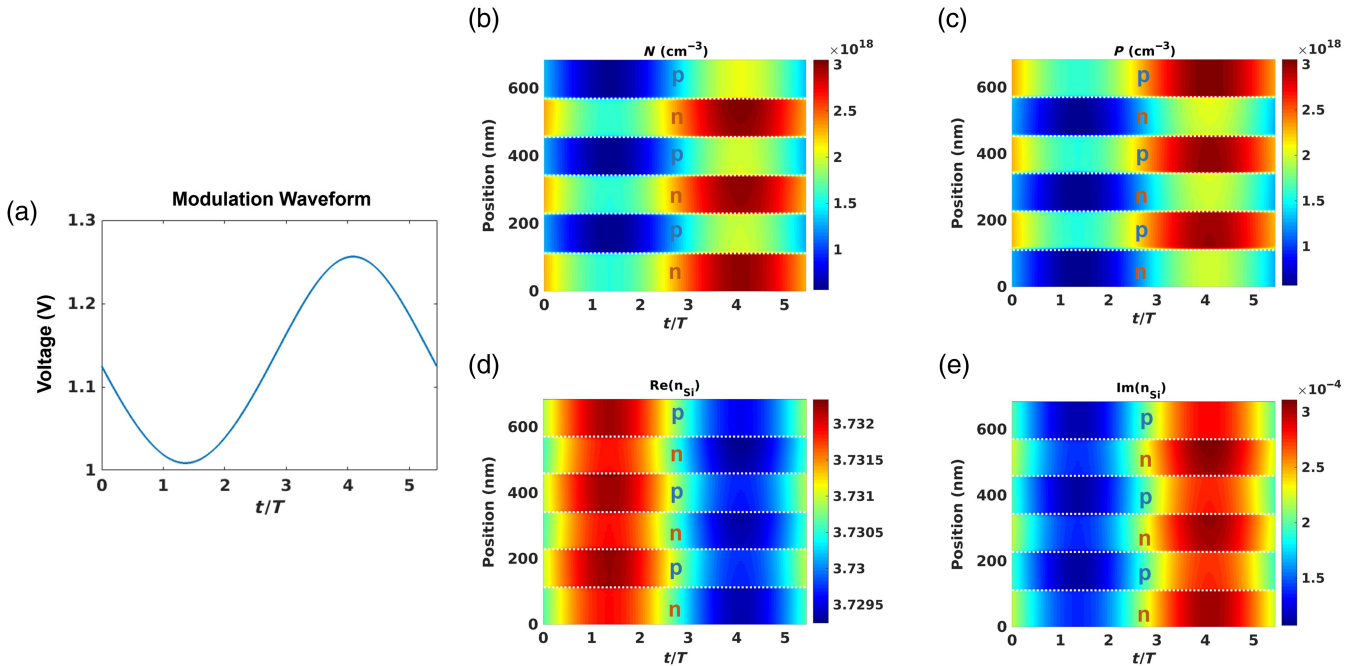


Fig. 3 Space–time modulation of the high- Q metasurface. (a) The profile of the sinusoidal modulation waveform with time-reversal symmetry that is applied to the metasurface. The spatial distributions of the (b) electron and (c) hole carrier concentrations inside the multijunction p–n layers as functions of time depicted in one modulation cycle. (d) The real and (e) imaginary parts of the refractive index within the multijunction p–n layers as functions of time and space in one modulation cycle obtained at the operating wavelength of 1548 nm. The refractive index is sinusoidally modulated between 3.7295 and 3.7325. The white dashed lines demarcate the boundaries between the p-type and n-type regions.

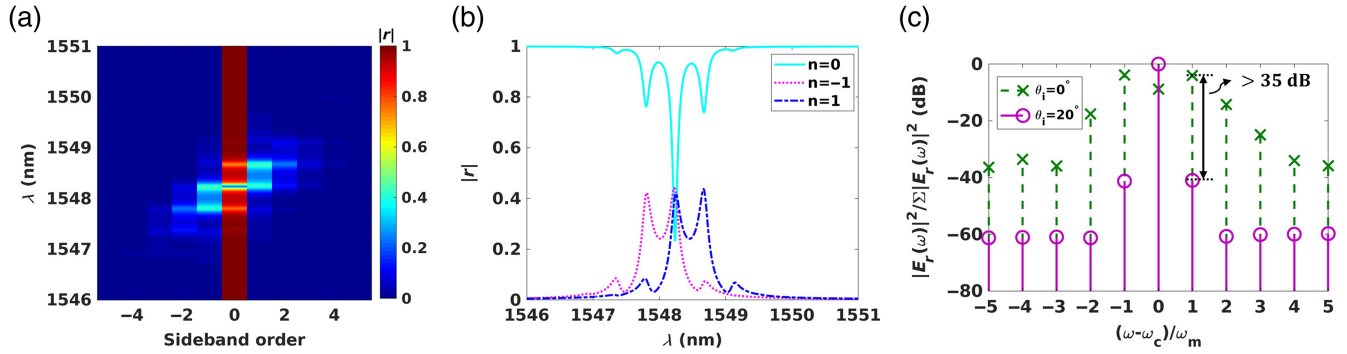


Fig. 4 Nonadiabatic frequency conversion performance of the normally illuminated ultrahigh- Q spatiotemporal metasurface under time reversal. (a) The output spectrum of the reflection coefficient at the generated sidebands as a function of sideband order (n) and the incident wavelength. (b) The reflection amplitude at the fundamental ($n = 0$), first-order upconverted ($n = +1$), and first-order downconverted ($n = -1$) sidebands as functions of incident wavelengths. (c) The normalized output spectrum of the reflected light when the space–time metasurface is under normal ($\theta_i = 0$ deg) and oblique ($\theta_i = 20$ deg) illuminations. An isolation level more than 35 dB is observed.

lower and upper bounds of the applied bias voltage and ΔV is the modulation depth. The upper and lower bounds for the modulation waveform are chosen such that they assure the uniform distribution of the electrons and holes within the p–n multijunction. Further details in this regard are provided in Sec. S7 in the [Supplementary Material](#). Figures 3(b) and 3(c) are the spatial distribution of the electrons and holes along the height of the SWG within a modulation cycle, respectively. The dashed lines demarcate the boundaries between the p-type and n-type regions. It is observed that upon applying the bias voltage, the electrons and holes are redistributed according to the magnitude and trajectory of the modulation waveform. Therefore, the carrier concentrations are modulated sinusoidally as functions of time through consecutive accumulation and depletion. Progressing in time, when the bias voltage becomes smaller than the DC voltage, the concentrations of electrons and holes decrease in the n-type and p-type regions. On the contrary, upon increasing the bias voltage above the DC level at the second half of the modulation cycle, the charge carriers start to accumulate within the p and n regions. It should be noted that the length of the SWGs along the y direction can result in modulation of the charge carriers in the lateral direction by moving away from the contact pads where the bias voltage is applied. Therefore, the footprint of the SWGs should be chosen to be compact in practice ($< 10 \mu\text{m}$) to avoid the carrier density change along the lateral direction that impacts the electro-optical performance of the metasurface and to minimize the RC time delay, which increases the response time. The spatial distributions of the real and imaginary parts of the refractive index in the multijunction p–n structure are obtained as functions of time within one modulation cycle at the operating wavelength of $\lambda = 1548.2$ nm; the results are shown in Figs. 3(d) and 3(e). It can be observed that for the bias voltage sinusoidally modulating between 1 and 1.25 V, the real part of the refractive index indicates the change of ≈ -0.003 , and the imaginary part remains below 3×10^{-4} . The small imaginary part is attained due to the moderate background doping of p- and n-type regions.

After characterizing the refractive index of the p–n multijunction, we employ RSTWA to calculate the electro-optical

response of the space–time metasurface to the modulation waveform depicted in Fig. 3(a). In order to account for nonuniformities of the permittivity according to the results in Figs. 3(d) and 3(e), we rigorously take into account their spatial distribution by discretization of the SWGs into several sublayers with homogeneous permittivity along the vertical direction. The number of sublayers is chosen to ensure the converged results, as shown in Sec. S7 in the [Supplementary Material](#). Figure 4(a) depicts the reflection amplitude spectra of the high Q -factor space–time metasurface as a function of sideband order and incident wavelength. It can be clearly seen from the result that when the incident wavelength strays away from the resonance, the output spectrum becomes highly asymmetric despite the symmetric waveform that is utilized for the excitation. In particular, for an incident light coming at the wavelength of 1548.7 nm, the power is substantially upconverted, and the downconversion is strongly suppressed. On the other hand, for the incident wavelengths below the resonance, namely, 1547.8 nm, the upconverted signal is strongly suppressed, and power is mainly downconverted. To provide better insight, we have plotted the reflection amplitude as a function of wavelength at the fundamental frequency and the first-order up- and downconverted sidebands in Fig. 4(b). For the upconverted sideband ($n = +1$), we can observe two reflection peaks at the resonant wavelength ($\lambda = 1548.2$ nm) and $\lambda = 1548.7$ nm that correspond to the up-modulation of the resonant frequency such that $\omega = \omega_r + \omega_m$. At the downconversion ($n = -1$), the reflection peaks are located at resonant wavelength ($\lambda = 1548.2$ nm) and its down-modulation ($\omega = \omega_r - \omega_m$), which corresponds to the wavelength $\lambda = 1547.8$ nm. At resonant wavelength, the reflection peaks at the upconverted and downconverted sidebands are degenerate, i.e., at the same wavelength. However, at off-resonance wavelengths, the degeneracy of the peaks is lifted, and they are shifted in different directions at the opposite sides of the spectrum. This is thanks to the high Q -factor of the metasurface paradigm, which induces the nonadiabatic modulation and leads to a well-separated sideband orders in the spectral domain and paves the way toward achieving the nonreciprocal response under time reversal. To demonstrate the capability of

our proposed space–time metasurface in power isolation between two arbitrary ports, we explored the output spectrum by exciting the metasurface under normal and oblique incidences, where the incident angles are adjusted to 0 deg and 20 deg. Figure 4(c) shows the results in which the output spectrum of the reflected light at port 1 (0 deg) and port 2 (20 deg) are calculated in logarithmic scale by taking the Fourier transform of the time-domain reflection coefficient; the spectra are normalized to the total scattered intensity from all the sidebands and the fundamental frequency. The operating frequency for the metasurface under normal illumination is at $\lambda = 1548.2$ nm, and it is adjusted to $\lambda = 1547.8$ nm for the oblique incidence. The difference between their corresponding angular frequencies is ω_m , which is considered to minimize the interference between the two ports. As can be seen from Fig. 4(c), the level of the upconverted reflected light from the space–time metasurface under normal incidence at port 1 is at least 35 dB larger than the one at port 2 under oblique incidence. This shows a great isolation between the two ports.

It should be noted that the proposed unit cell is designed for nonreciprocal operation between any two arbitrary directions. This is in contrast to the previous magnetless time-modulated paradigm for power isolation in Ref. 52, wherein the restriction is imposed on the frequencies of the two supported nonlocal resonant modes and limits the isolation between only two specific directions. In addition, the proposed unit cell is composed of a single metasurface layer that allows for power isolation by leveraging the sharp contrast between the fundamental and upconverted signal that is achieved due to the high- Q resonator. This is unlike the recent study in Ref. 87, which employs an additional layer as a filter to increase the isolation level between the two ports. It is also worth mentioning that we have not made any effort to optimize the modulation waveform in order to increase the isolation level, and a simple sinusoidal waveform is employed that yields a noticeable conversion into a higher-order sideband. However, in Sec. S8 in the [Supplementary Material](#), we have shown that by optimizing the modulation waveform, the isolation level can be further increased to 40 dB.

4 Gradient Metasurface for Nonreciprocal Beam Steering

In this section, we employ the proposed unit cell for constructing the time-modulated reflectarray that exhibits a nonreciprocal response. Toward this aim, the sinusoidal modulation waveform indicated in Fig. 3(a) as well as the modulation-induced progressive phase delays are applied across the metasurface to render a phase gradient reflectarray in space and time. The modulation profile can be synthesized by the arbitrary waveform generator (AWG). The measurement of the sidebands can be done directly by the optical spectrum analyzers if they are separated at a few gigahertz intervals or can be done with photo-detection and use of RF spectrum analyzers if their separation is <1 GHz. The RF phase shifts required for beam steering toward the desired angle can be impacted by introducing the phase shift in different channels of the AWG addressing the array elements. Such an RF biasing network for implementing the time-modulated metasurface can lead to cross talk between the adjacent metasurface elements.⁸⁸ However, the signal distortion due to the cross talk can be minimized by adjusting the interelement spacing or coating the elements with a capping insulator layer that can further isolate the adjacent elements.

To verify the capability of the proposed space–time gradient metasurface for free-space power isolation, we consider a periodic supercell that consists of five time-varying unit cells that are arranged along the x axis. The separation distance between the elements is $\Lambda = 1007$ nm, which is around $\approx \lambda/1.5$ at the operating wavelength. The structure is normally illuminated by the y -polarized plane wave. The modulation waveform is kept unchanged, as depicted in Fig. 3(a), whereas the progressive phase delay of $\alpha(x) = -k_0 x \sin(\theta_s)$ is implemented across the metasurface in accordance with the requirement for achieving the target steering angle of θ_s at the output. The steering angle is set to $\theta_s = 20$ deg for our studies. It is worth mentioning that the progressive phase shift imprinted on the wavefront of the reflected light at the sidebands is dispersionless and spans over the complete 2π range. This resembles the Pancharatnam–Berry phase shift, which occurs in half-wave plate converters upon polarization conversion and makes the space–time metasurfaces break away from the limitations caused by the dispersive nature of resonant unit cells. In addition, the phase profile of the upconverted signal provides a negative phase shift with respect to the downconverted case. This can be implied from Eq. (14) in Ref. 84, which shows the imprinted phase gradients at the sidebands with the opposite orders are conjugate. The spatiotemporal permittivity change of the α -Si SWG, which results from the sinusoidal modulation waveform, can be described as $\epsilon_{\text{SWG}} = \epsilon_{\text{dc}} + \Delta\epsilon \sin[\omega_m t + \alpha(x)]$, where $\Delta\epsilon$ is the modulation depth and defines the deviation of the permittivity with respect to the unbiased configuration, which is set to 0.008 in accordance with Fig. 3(d). The desired output spectrum of the sidebands is maintained by adequately tailoring the modulation depth that controls the level of the reflected power at different sidebands, as depicted in Fig. 4(a).

In order to establish the isolation between the two ports in free space, which are selected as normal direction and $\theta_s = 20$ deg, we apply the modulation waveform and required phase gradient across the reflectarray. Under time reversal, the incident light can undergo an up- or downconversion and be steered toward the different spatial pathways defined by the imprinted phase gradient. In the account of the nonadiabatic frequency conversion performance, for the incoming light, whose wavelength is longer than the resonant wavelength, the downconversion is strongly suppressed, while for the light with the incident wavelength shorter than the resonant, the upconversion is eliminated. Figures 5(a)–5(d) illustrate the wavefronts of the reflected light at the fundamental frequency and its upconversion, when the reflectarray is illuminated by the normal and oblique beams. For the sake of simplicity, the normal and oblique directions at $\theta = 0$ deg and $\theta = 20$ deg are called port 1 and port 2, respectively. As is clearly observed, for the incoming light from port 1 and at resonant frequency (ω_r), the light is reflected back to port 1, since the direction of the fundamental frequency is governed by the specular reflection and cannot be actively tuned by changing the modulation-induced phase shift.⁸⁴ However, the reflected light at the upconverted sideband ($\omega_r + \omega_m$) is steered toward port 2 at $\theta = 20$ deg. The perturbations in the wavefront of the magnetic field in Fig. 5(b) show that the amplitude at the sideband does not remain constant at the nonadiabatic regime of modulation despite the adiabatic regime. However, the anomalous reflection of light to port 2 at the first-order sideband confirms that the dispersionless phase shift spanning on 2π persists in this regime. Figures 5(c) and 5(d) show the reflected light upon exciting the reflectarray by the

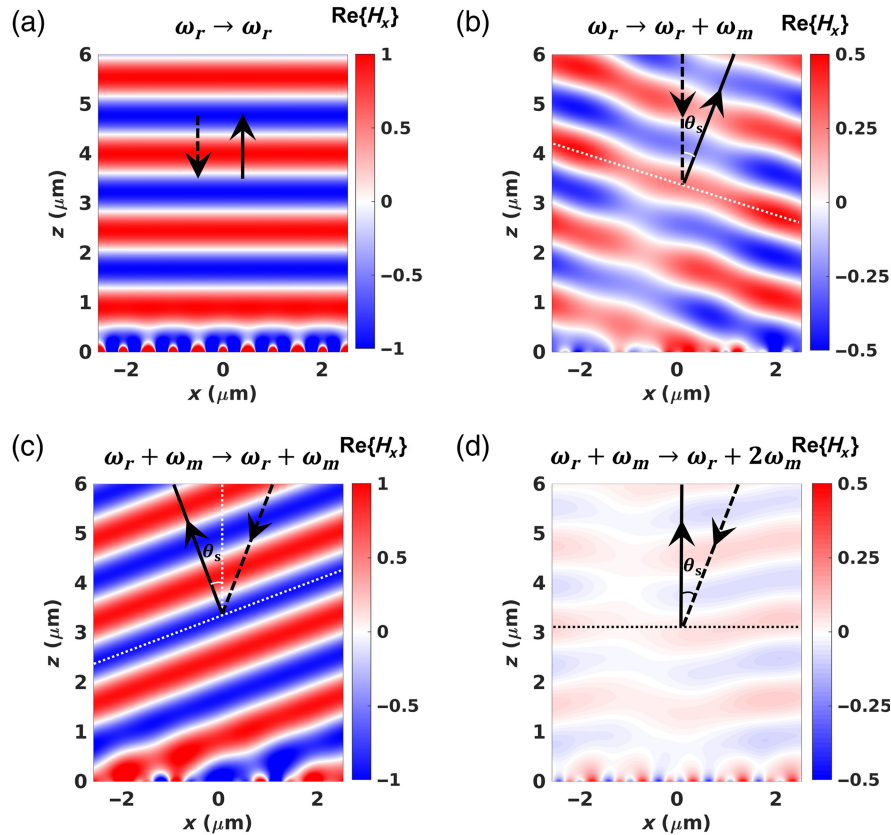


Fig. 5 Optical power isolation in free space. The wavefronts of the reflected light from the gradient space–time metasurface at the fundamental and first-order upconverted sidebands when the metasurface is illuminated by (a), (b) normal light coming from port 1 and (c), (d) oblique incidence coming from port 2. At resonant frequency ($\omega = \omega_r$), the upconverted normally incident light is steered toward port 2 ($\theta = 20$ deg). The light incoming from port 2 at $\omega_r + \omega_m$ is bent toward port 1 at $\theta = 0$ deg upon upconversion, while its amplitude is strongly suppressed. The color bars are rescaled to provide a fair comparison. The magnetic field level in (d) varies between -0.01 and 0.01 .

incoming light from port 2. The frequency of the incident light is identical to upmodulation of the resonant frequency, and therefore its corresponding wavelength is shorter than the resonant. According to Fig. 4(a), in this case, the upconversion of the incident light should be suppressed. Similar to the previous case, at the fundamental frequency ($\omega_r + \omega_m$), the incident light coming from port 2 undergoes a specular reflection, and its spatial pathway is bent to the symmetrically opposite angle under oblique incidence ($\theta = -20$ deg), which is well separated from port 1. On the other hand, the upconverted light at $\omega_r + 2\omega_m$ is steered toward its initial pathway at port 1, due to experiencing a conjugate modulation-induced phase gradient, while its amplitude is significantly attenuated because of the nonadiabatic frequency conversion performance, as was expected. It can be concluded from the results in Fig. 5 that the incoming power from port 1 can be mainly coupled to port 2 under time reversal, while the power coupling from port 2 into port 1 is significantly small, which ensures optical power isolation in free space between the two ports. This concept can be easily expanded to establish isolated links between any arbitrary ports in free space. As is shown in Fig. 4(c), the normalized isolation level between the ports is calculated as ≈ 35 dB. It should be noted that the reciprocal metasurface would have steered the beam to its initial direction without any change in its amplitude.

5 Conclusion

In this paper, we numerically demonstrated the realization of high Q -factor space–time gradient metasurface operating at the NIR regime for optical power isolation. For this purpose, we considered an a -Si SWG on top of the SiO_2 substrate and DBR as the metasurface building block. To apply the time-varying biasing, the SWGs are configured as multijunction p–n layers with moderate doping, which enables index modulation through electrorefraction induced by carrier accumulation within the entire SWG volume. The structural parameters of the metasurface are adjusted such that it supports a localized higher-order Mie resonance that is characterized as a magnetic octupole. The Q -factor of the resonance is calculated as 11,876, which gives rise to the photon lifetime within the resonator such that the time scale of the optical oscillation becomes comparable with the modulation cycle and renders the nonadiabatic modulation process. The frequency conversion performance of the space–time metasurface in nonadiabatic modulation regime demonstrates nonreciprocal response under time reversal and allows for strong suppression of the frequency upconversion (downconversion) upon exciting the metasurface by upmodulated (downmodulated) incident light. By introducing the modulation-induced phase delay between the individual elements of

the nonreciprocal metasurface, a phase gradient reflectarray is rendered in space and time that allows for optical power isolation between any two arbitrary ports in free space. We have considered the two ports as $\theta = 0$ deg (port 1) and $\theta = 20$ deg (port 2), respectively. The incoming light from port 1 is upconverted ($\omega_r \rightarrow \omega_r + \omega_m$) and steered toward port 2 by virtue of the modulation-induced phase shift. On the other hand, the upmodulated incident light at port 2 undergoes an upconversion ($\omega_r + \omega_m \rightarrow \omega_r + 2\omega_m$) and points toward a well-separated angle at port 1 due to experiencing a conjugate modulation-induced phase gradient. On account of nonadiabatic frequency conversion performance, the reflected light at port 1 is substantially suppressed, while the dominant portion of the reflected field that does not undergo frequency conversion bends toward the specular reflection angle. The normalized isolation level between the ports is calculated as ≈ 35 dB.

Disclosures

The authors declare no conflicts of interest.

Code and Data Availability

Structural parameters and simulated and experimental data have been provided within the main text and [Supplementary Material](#) of this paper. All the other data that support the findings of this study are available from the corresponding author upon reasonable request.

Acknowledgments

This work was supported in part by Air Force Office of Scientific Research (Grant No. FA9550-18-1-0354). Raana Sabri would like to acknowledge Dr. Mohammad Mahdi Salary for his contribution.

References

- N. Yu et al., “Light propagation with phase discontinuities: generalized laws of reflection and refraction,” *Science* **334**(6054), 333–337 (2011).
- N. Yu and F. Capasso, “Flat optics with designer metasurfaces,” *Nat. Mater.* **13**(2), 139–150 (2014).
- A. M. Wong and G. V. Eleftheriades, “Perfect anomalous reflection with a bipartite Huygens’ metasurface,” *Phys. Rev. X* **8**(1), 011036 (2018).
- M. Decker et al., “High-efficiency dielectric Huygens’ surfaces,” *Adv. Opt. Mater.* **3**(6), 813–820 (2015).
- S. Divitt et al., “Ultrafast optical pulse shaping using dielectric metasurfaces,” *Science* **364**(6443), 890–894 (2019).
- P. C. Wu et al., “Broadband wide-angle multifunctional polarization converter via liquid-metal-based metasurface,” *Adv. Opt. Mater.* **5**(7), 1600938 (2017).
- R. Sabri, A. Forouzmand, and H. Mosallaei, “Genetically optimized dual-wavelength all-dielectric metasurface based on double-layer epsilon-near-zero indium-tin-oxide films,” *J. Appl. Phys.* **128**(22), 223101 (2020).
- W. T. Chen et al., “A broadband achromatic metalens for focusing and imaging in the visible,” *Nat. Nanotechnol.* **13**(3), 220–226 (2018).
- A. Pors et al., “Broadband focusing flat mirrors based on plasmonic gradient metasurfaces,” *Nano Lett.* **13**(2), 829–834 (2013).
- A. M. Shaltout, V. M. Shalaev, and M. L. Brongersma, “Spatiotemporal light control with active metasurfaces,” *Science* **364**(6441), eaat3100 (2019).
- T. Cui, B. Bai, and H.-B. Sun, “Tunable metasurfaces based on active materials,” *Adv. Funct. Mater.* **29**(10), 1806692 (2019).
- P. Thureja et al., “Toward a universal metasurface for optical imaging, communication, and computation,” *Nanophotonics* **11**(17), 3745–3768 (2022).
- M. Elsayy et al., “Universal active metasurfaces for ultimate wavefront molding by manipulating the reflection singularities,” *Laser Photonics Rev.* **17**(7), 2200880 (2022).
- T. Lewi, N. A. Butakov, and J. A. Schuller, “Thermal tuning capabilities of semiconductor metasurface resonators,” *Nanophotonics* **8**(2), 331–338 (2018).
- S.-Y. Lee et al., “Thermal actuated solid tunable lens,” *IEEE Photonics Technol. Lett.* **18**(21), 2191–2193 (2006).
- M. Rahmani et al., “Reversible thermal tuning of all-dielectric metasurfaces,” *Adv. Funct. Mater.* **27**(31), 1700580 (2017).
- G. Cocorullo, F. Della Corte, and I. Rendina, “Temperature dependence of the thermo-optic coefficient in crystalline silicon between room temperature and 550 K at the wavelength of 1523 nm,” *Appl. Phys. Lett.* **74**(22), 3338–3340 (1999).
- E. Arbabi et al., “MEMS-tunable dielectric metasurface lens,” *Nat. Commun.* **9**(1), 812 (2018).
- M. R. Shcherbakov et al., “Ultrafast all-optical tuning of direct-gap semiconductor metasurfaces,” *Nat. Commun.* **8**(1), 17 (2017).
- P. C. Wu et al., “Dynamic beam steering with all-dielectric electro-optic III–V multiple-quantum-well metasurfaces,” *Nat. Commun.* **10**(1), 3654 (2019).
- H. Chung et al., “Electrical phase modulation based on mid-infrared intersubband polaritonic metasurfaces,” *Adv. Sci.* **10**(16), 2207520 (2023).
- C. H. Chu et al., “Active dielectric metasurface based on phase-change medium,” *Laser Photonics Rev.* **10**(6), 986–994 (2016).
- S.-Q. Li et al., “Phase-only transmissive spatial light modulator based on tunable dielectric metasurface,” *Science* **364**(6445), 1087–1090 (2019).
- A. L. Holsteen, A. F. Cihan, and M. L. Brongersma, “Temporal color mixing and dynamic beam shaping with silicon metasurfaces,” *Science* **365**(6450), 257–260 (2019).
- M. M. Salary, S. Farazi, and H. Mosallaei, “A dynamically modulated all-dielectric metasurface doublet for directional harmonic generation and manipulation in transmission,” *Adv. Opt. Mater.* **7**(23), 1900843 (2019).
- G. K. Shirmanesh et al., “Electro-optically tunable multifunctional metasurfaces,” *ACS Nano* **14**(6), 6912–6920 (2020).
- R. Sokhoyan et al., “Electrically tunable conducting oxide metasurfaces for high power applications,” *Nanophotonics* **12**(2), 239–253 (2023).
- A. Forouzmand et al., “Tunable all-dielectric metasurface for phase modulation of the reflected and transmitted light via permittivity tuning of indium tin oxide,” *Nanophotonics* **8**(3), 415–427 (2019).
- R. Sabri, A. Forouzmand, and H. Mosallaei, “Multi-wavelength voltage-coded metasurface based on indium tin oxide: independently and dynamically controllable near-infrared multi-channels,” *Opt. Express* **28**(3), 3464–3481 (2020).
- S. Vatani, H. Taleb, and M. K. Moravvej-Farshi, “Optical modulation via guided-mode resonance in an ITO-loaded distributed Bragg reflector topped with a two-dimensional grating,” *IEEE J. Sel. Top. Quantum Electron.* **27**(3), 1–7 (2021).
- J. Park et al., “Dynamic thermal emission control with INAS-based plasmonic metasurfaces,” *Sci. Adv.* **4**(12), eaat3163 (2018).
- R. Sabri and H. Mosallaei, “Inverse design of perimeter-controlled INAS-assisted metasurface for two-dimensional dynamic beam steering,” *Nanophotonics* **11**(20), 4515–4530 (2022).
- P. Ni et al., “Gate-tunable emission of exciton–plasmon polaritons in hybrid MoS₂-gap-mode metasurfaces,” *ACS Photonics* **6**(7), 1594–1601 (2019).
- M. Li et al., “Excitonic beam steering in an active van der Waals metasurface,” arXiv:2211.09297 (2022).

35. A. Forouzmard and H. Mosallaei, “A tunable semiconductor-based transmissive metasurface: dynamic phase control with high transmission level,” *Laser Photonics Rev.* **14**(6), 1900353 (2020).
36. G. Kafaie Shirmanesh et al., “Dual-gated active metasurface at 1550 nm with wide (>300°) phase tunability,” *Nano Lett.* **18**(5), 2957–2963 (2018).
37. J. Park et al., “Dynamic reflection phase and polarization control in metasurfaces,” *Nano Lett.* **17**(1), 407–413 (2017).
38. R. Sabri, M. M. Salary, and H. Mosallaei, “Single sideband suppressed carrier modulation with spatiotemporal metasurfaces at near-infrared spectral regime,” *J. Lightwave Technol.* **40**(12), 3802–3813 (2022).
39. J. Park et al., “An over-coupled phase-change metasurface for efficient reflection phase modulation,” *Adv. Opt. Mater.* **8**(20), 2000745 (2020).
40. M. M. Salary and H. Mosallaei, “Tunable all-dielectric metasurfaces for phase-only modulation of transmitted light based on quasi-bound states in the continuum,” *ACS Photonics* **7**(7), 1813–1829 (2020).
41. Y. Horie et al., “High-speed, phase-dominant spatial light modulation with silicon-based active resonant antennas,” *ACS Photonics* **5**(5), 1711–1717 (2017).
42. Y. Akahane et al., “High-q photonic nanocavity in a two-dimensional photonic crystal,” *Nature* **425**(6961), 944–947 (2003).
43. L. Huang et al., “Pushing the limit of high-q mode of a single dielectric nanocavity,” *Adv. Photonics* **3**(1), 016004 (2021).
44. E. Klopfer et al., “Dynamic focusing with high-quality-factor metalenses,” *Nano Lett.* **20**(7), 5127–5132 (2020).
45. M. Taghavi and H. Mosallaei, “Increasing the stability margins using multi-pattern metasails and multi-modal laser beams,” *Sci. Rep.* **12**(1), 20034 (2022).
46. V. Mylnikov et al., “Lasing action in single subwavelength particles supporting supercavity modes,” *ACS Nano* **14**(6), 7338–7346 (2020).
47. R. Berté et al., “Permittivity-asymmetric quasi-bound states in the continuum,” *Nano Lett.* **23**(7), 2651–2658 (2023).
48. C. U. Hail et al., “High quality factor metasurfaces for two-dimensional wavefront manipulation,” arXiv:2212.05647 (2022).
49. S. Taravati and G. V. Eleftheriades, “Full-duplex nonreciprocal beam steering by time-modulated phase-gradient metasurfaces,” *Phys. Rev. Appl.* **14**(1), 014027 (2020).
50. M. M. Salary, S. Jafar-Zanjani, and H. Mosallaei, “Nonreciprocal optical links based on time-modulated nanoantenna arrays: full-duplex communication,” *Phys. Rev. B* **99**(4), 045416 (2019).
51. Y. Hadad, D. L. Sounas, and A. Alu, “Space-time gradient metasurfaces,” *Phys. Rev. B* **92**(10), 100304 (2015).
52. Y. Shi, S. Han, and S. Fan, “Optical circulation and isolation based on indirect photonic transitions of guided resonance modes,” *ACS Photonics* **4**(7), 1639–1645 (2017).
53. X. Guo et al., “Nonreciprocal metasurface with space–time phase modulation,” *Light Sci. Appl.* **8**(1), 123 (2019).
54. D. L. Sounas, C. Caloz, and A. Alu, “Giant non-reciprocity at the subwavelength scale using angular momentum-biased metamaterials,” *Nat. Commun.* **4**(1), 2407 (2013).
55. M. M. S. Shahrababaki, “Space-time photonic metamaterials,” PhD thesis, Northeastern University (2020).
56. Y. Shi, Z. Yu, and S. Fan, “Limitations of nonlinear optical isolators due to dynamic reciprocity,” *Nat. Photonics* **9**(6), 388–392 (2015).
57. D. Jalas et al., “What is—and what is not—an optical isolator,” *Nat. Photonics* **7**(8), 579–582 (2013).
58. Z. Wang et al., “Gyrotropic response in the absence of a bias field,” *Proc. Natl. Acad. Sci., U. S. A.* **109**(33), 13194–13197 (2012).
59. G. Lavigne, T. Kodaera, and C. Caloz, “Metasurface magnetless specular isolator,” *Sci. Rep.* **12**(1), 5652 (2022).
60. Y. Hadad et al., “Extreme and quantized magneto-optics with graphene meta-atoms and metasurfaces,” *ACS Photonics* **1**(10), 1068–1073 (2014).
61. J. W. Zang et al., “Nonreciprocal wavefront engineering with time-modulated gradient metasurfaces,” *Phys. Rev. Appl.* **11**(5), 054054 (2019).
62. M. Bourkov et al., “Time-modulated patch antennas with nonreciprocal polarization handedness,” in *IEEE Int. Symp. Antenn. and Propag. and North Amer. Radio Sci. Meet.*, IEEE, pp. 745–746 (2020).
63. V. Chistyakov et al., “Tunable magnetless optical isolation with twisted Weyl semimetals,” arXiv:2304.09271 (2023).
64. A. Howes et al., “Dynamic transmission control based on all-dielectric Huygens metasurfaces,” *Optica* **5**(7), 787–792 (2018).
65. E. Tiguntseva et al., “Room-temperature lasing from Mie-resonant nonplasmonic nanoparticles,” *ACS Nano* **14**(7), 8149–8156 (2020).
66. I. H. Malitson, “Interspecimen comparison of the refractive index of fused silica,” *JOSA* **55**(10), 1205–1209 (1965).
67. R. Soref and B. Bennett, “Electrooptical effects in silicon,” *IEEE J. Quantum Electron.* **23**(1), 123–129 (1987).
68. D. Hohlfeld and H. Zappe, “An all-dielectric tunable optical filter based on the thermo-optic effect,” *J. Opt. A Pure Appl. Opt.* **6**(6), 504 (2004).
69. Y. Horie et al., “Active dielectric antenna for phase only spatial light modulation,” in *Conf. Lasers and Electro-Opt. (CLEO)*, Optica Publishing Group, pp. 1–2 (2016).
70. M. H. MacDougal et al., “Design and fabrication of VCSELS with al/sub x/o/sub y/-GAAS DBRS,” *IEEE J. Sel. Top. Quantum Electron.* **3**(3), 905–915 (1997).
71. H. Lira et al., “Electrically driven nonreciprocity induced by interband photonic transition on a silicon chip,” *Phys. Rev. Lett.* **109**(3), 033901 (2012).
72. S. Inampudi et al., “Rigorous space-time coupled-wave analysis for patterned surfaces with temporal permittivity modulation,” *Opt. Mater. Express* **9**(1), 162–182 (2019).
73. A. Forouzmard and H. Mosallaei, “Electro-optical amplitude and phase modulators based on tunable guided-mode resonance effect,” *ACS Photonics* **6**(11), 2860–2869 (2019).
74. E. Klopfer et al., “High-quality-factor silicon-on-lithium niobate metasurfaces for electro-optically reconfigurable wavefront shaping,” *Nano Lett.* **22**(4), 1703–1709 (2022).
75. R. Sokhoyan et al., “All-dielectric high-q dynamically tunable transmissive metasurfaces,” arXiv:2309.08031 (2023).
76. E. A. Gurvitz et al., “The high-order toroidal moments and anapole states in all-dielectric photonics,” *Laser Photonics Rev.* **13**(5), 1800266 (2019).
77. A. Hassanfiroozi et al., “Toroidal-assisted generalized Huygens’ sources for highly transmissive plasmonic metasurfaces,” *Laser Photonics Rev.* **16**(6), 2100525 (2022).
78. A. Hassanfiroozi et al., “Vertically-stacked discrete plasmonic meta-gratings for broadband space-variant metasurfaces,” *Adv. Opt. Mater.* **11**(8), 2202717 (2023).
79. R. Alaei, C. Rockstuhl, and I. Fernandez-Corbaton, “An electromagnetic multipole expansion beyond the long-wavelength approximation,” *Opt. Commun.* **407**, 17–21 (2018).
80. P. D. Terekhov et al., “Multipole analysis of dielectric metasurfaces composed of nonspherical nanoparticles and lattice invisibility effect,” *Phys. Rev. B* **99**(4), 045424 (2019).
81. M. H. Pfeiffer et al., “Ultra-smooth silicon nitride waveguides based on the damascene reflow process: fabrication and loss origins,” *Optica* **5**(7), 884–892 (2018).
82. Y. Takahashi et al., “High-q nanocavity with a 2-ns photon lifetime,” *Opt. Express* **15**(25), 17206–17213 (2007).
83. R. Sabri, M. M. Salary, and H. Mosallaei, “Broadband continuous beam-steering with time-modulated metasurfaces in the near-infrared spectral regime,” *APL Photonics* **6**(8), 086109 (2021).
84. R. Sabri, M. M. Salary, and H. Mosallaei, “Quasi-static and time-modulated optical phased arrays: beamforming analysis and comparative study,” *Adv. Photonics Res.* **2**(9), 2100034 (2021).

85. K. Y. Lee et al., “Multiple PN junction subwavelength gratings for transmission-mode electro-optic modulators,” *Sci. Rep.* **7**(1), 46508 (2017).
86. M. Nedeljkovic, R. Soref, and G. Z. Mashanovich, “Free-carrier electrorefraction and electroabsorption modulation predictions for silicon over the 1–14- μm infrared wavelength range,” *IEEE Photonics J.* **3**(6), 1171–1180 (2011).
87. D. Ramaccia et al., “Electromagnetic isolation induced by time-varying metasurfaces: nonreciprocal Bragg grating,” *IEEE Antenn. Wirel. Propag. Lett.* **19**(11), 1886–1890 (2020).
88. P. Thureja et al., “Space-time modulated metasurfaces for steering of frequency-shifted beams,” in *CLEO: Fundam. Sci.*, Optica Publishing Group, pp. FTu4D.5 (2023).
89. P. D. Terekhov et al., “Multipolar response of nonspherical silicon nanoparticles in the visible and near-infrared spectral ranges,” *Phys. Rev. B* **96**(3), 035443 (2017).
90. A. B. Evlyukhin and B. N. Chichkov, “Multipole decompositions for directional light scattering,” *Phys. Rev. B* **100**(12), 125415 (2019).
91. Lumerical Inc., Charge Solution, A Commercial Professional Software, <http://www.lumerical.com> (2023).

Biographies of the authors are not available.